

Modular strategies for spatial mapping of diverse cell type data of the mouse brain

⁴ Nicholas J. Tustison¹, Min Chen², Fae N. Kronman³, Jeffrey T. Duda², Clare Gamlin⁴, Mia
⁵ G. Tustison, Michael Kunst⁴, Rachel Dalley⁴, Staci Sorenson⁴, Quanxin Wang⁴, Lydia Ng⁴,
⁶ Yongsoo Kim³, and James C. Gee²

¹Department of Radiology and Medical Imaging, University of Virginia, Charlottesville, VA

²Department of Radiology, University of Pennsylvania, Philadelphia, PA

³Department of Neural and Behavioral Sciences, Penn State University, Hershey, PA

⁴Allen Institute for Brain Science, Seattle, WA

11 _____

12 Corresponding authors:

13

14 Nicholas J. Tustison, DSc

15 Department of Radiology and Medical Imaging

16 University of Virginia

17 ntustison@virginia.edu

J. C. G. BLOD

19 James C. Gee, PhD
20 Department of Radiology

20 Department of Radiol
21 University of Pennsylvania

21 University of Pe
22 geo@upenn.edu

²³ **Abstract**

²⁴ Large-scale, international collaborative efforts by members of the BRAIN Initiative Cell
²⁵ Census Network (BICCN) consortium have recently begun aggregating the most compre-
²⁶ hensive reference database to date for diverse cell type profiling of the mouse brain, which
²⁷ encompasses over 40 different multi-modal profiling techniques from more than 30 research
²⁸ groups. One central challenge for this integrative effort across different investigators and
²⁹ laboratories has been the need to map these unique datasets into common reference spaces
³⁰ such that the spatial, structural, and functional information from different cell types can be
³¹ jointly analyzed across modalities. However, significant variations in the acquisition, tissue
³² processing, and imaging techniques across data types makes mapping such diverse data a
³³ multifarious problem. Different data types exhibit unique tissue distortion and signal char-
³⁴ acteristics that precludes a single mapping strategy from being generally applicable across
³⁵ all cell type data. Diverse, and often specialized, mapping approaches are needed to address
³⁶ the unique barriers present in each modality. This work highlights modular atlas mapping
³⁷ strategies developed across three separate BICCN studies using the Advanced Normalization
³⁸ Tools Ecosystem (ANTsX) to map spatial transcriptomic (MERFISH) and high-resolution
³⁹ morphology (fMOST) mouse brain data into the Allen Common Coordinate Framework
⁴⁰ (AllenCCFv3), and developmental (MRI and LSFM) data into the Developmental Com-
⁴¹ mon Coordinate Framework (DevCCF). We discuss both common mapping strategies that
⁴² can be shared across modalities, and targeted strategies driven by specific challenges from
⁴³ each data type. Novel open-source contributions are also made publicly available through
⁴⁴ ANTSX. These include a velocity flow-based approach for continuously mapping develop-
⁴⁵ mental trajectories such as that characterizing the DevCCF and an automated framework for
⁴⁶ determining structural morphology solely through the leveraging of publicly resources. Fi-
⁴⁷ nally, we provide general guidance to aid investigators in their efforts to tailor these strategies
⁴⁸ to address unique challenges in their data without the need to develop additional specialized
⁴⁹ software.

50 1 Introduction

51 Over the past decade there have been significant advancements in mesoscopic single-cell anal-
52 ysis of the mouse brain. It is now possible to track single neurons in mouse brains¹, observe
53 whole brain developmental changes on a cellular level², associate brain regions and tissues
54 with their genetic composition³, and locally characterize neural connectivity⁴. Much of these
55 scientific achievements have been made possible due to breakthroughs in high resolution cell
56 profiling and imaging techniques that permit submicron, multi-modal, 3D characterizations
57 of whole mouse brains. Among these include advanced techniques such as micro-optical
58 sectioning tomography⁶, tissue clearing^{1,7}, spatial transcriptomics⁹, and single-cell genomic
59 profiling¹⁰, which have greatly expanded the resolution and specificity of single-cell measure-
60 ments in the brain.

61 Recent efforts by the National Institutes of Health's Brain Research Through Advancing
62 Innovative Neurotechnologies (BRAIN) Initiative has pushed for large-scale, international
63 collaborative efforts to utilize these advanced single cell techniques to create a comprehensive
64 reference database for high-resolution transcriptomic, epigenomic, structural and imaging
65 data of the mouse brain. This consortium of laboratories and data centers, known as the
66 BRAIN Initiative Cell Census Network (BICCN), has to date archived datasets encompassing
67 over 40 different multi-modal profiling techniques from more than 30 research groups, each
68 providing unique characterizations of distinct cell types in the brain¹¹. Several of these
69 modalities have been further developed into reference atlases to facilitate spatial alignment
70 of individual brains and different data types into a common coordinate framework (CCF),
71 thus allowing diverse single-cell information to be integrated and analyzed in tandem. The
72 most notable of these atlases is the Allen Mouse Brain Common Coordinate Framework
73 (AllenCCFv3)¹², which serves as the primary target coordinate space to which the majority
74 of BICCN mouse data are mapped. Other atlases include modality-specific atlases¹³⁻¹⁵, and
75 spatiotemporal atlases^{16,17} for the developing mouse brain.

76 **1.1 Mouse brain mapping**

77 The cross-modality associations that can be learned from mapping different cell type data
78 into a CCF is critical for improving our understanding of the complex relationships between
79 cellular structure, morphology, and genetics in the brain. However, finding an accurate map-
80 ping between each individual mouse brain and a CCF is a challenging and heterogeneous task.
81 There is significant variance in the acquisition, fixation and imaging protocols across different
82 cell type data, and different tissue processing and imaging methods can potentially introduce
83 modality specific tissue distortion and signal differences^{18,19}. Certain modalities can have
84 poor intensity correspondence with the CCF, making image alignment less robust. Studies
85 targeting specific regions or cell types can lead to missing anatomical correspondences. Other
86 considerations include artifacts such as tissue distortion, holes, bubbles, folding, tears, and
87 missing sections in the data that often require manual correction^{20–23}. Given the diversity
88 of these challenges, it is unlikely any single mapping approach can be generally applicable
89 across all cell type data. Diverse, and often specialized, strategies are needed to address the
90 unique barriers present for mapping each modality.

91 Existing solutions to address mapping cell type data into the AllenCCFv3 falls broadly into
92 three main categories. The first consists of integrated processing platforms that directly
93 provide mapped data to the users. These include the Allen Brain Cell Atlas²⁴ for the Allen
94 Reference Atlas (ARA) and associated data, the Brain Architecture Portal²⁵ for combined
95 ex vivo radiology and histology data, OpenBrainMap²⁶ for connectivity data, and the Image
96 and Multi-Morphology Pipeline²⁷ for high resolution morphology data. These platforms
97 provide users online access to pre-processed, multi-modal cell type data that are already
98 mapped to the AllenCCFv3. The platforms are designed such that the data is interactively
99 manipulated by users through integrated visualization software that allow users to spatially
100 manipulate and explore each dataset within the mapped space. While highly convenient
101 for investigators who are interested in studying the specific modalities provided by these
102 platforms, these systems can be limited in flexibility and more general applicability. The
103 mapping software and pipelines are typically developed specifically with the data type and
104 platform in mind, and the software is limited public availability. Investigators will find it

¹⁰⁵ difficult to apply the same mapping to their own data without direct collaboration with the
¹⁰⁶ platform owners.

¹⁰⁷ The second category are specialized approaches specifically designed for mapping one or
¹⁰⁸ more modalities into a CCF. These approaches use combinations of specialized manual and
¹⁰⁹ automated processes that address specific challenges in each modality. Examples include ap-
¹¹⁰ proaches for mapping histology^{28–30}, magnetic resonance imaging (MRI)³⁷, micro-computed
¹¹¹ tomography (microCT)^{35,37}, light-sheet fluorescence microscopy (LSFM)^{34,36–39}, fluorescence
¹¹² micro-optical sectioning tomography (fMOST)^{15,40} and transcriptomic data^{41–43}. As special-
¹¹³ ized approaches, these techniques tend to boast higher mapping accuracy, robustness, and
¹¹⁴ ease of use when ran with applicable modalities. Conversely, their specialized designs often
¹¹⁵ rely on base assumptions regarding the data type that can make them rigid and difficult
¹¹⁶ to adapt for new modalities or unexpected artifacts and distortions in the data. Retooling
¹¹⁷ these specialize software to use with new data can require significant development, validation
¹¹⁸ time, and engineering expertise that may not be readily available for all investigators.

¹¹⁹ The last category are modular mapping approaches constructed using general image analy-
¹²⁰ sis toolkits, which are software packages that include varied collections of image processing,
¹²¹ segmentation and registration tools that have been previously developed, and validated for
¹²² multiple application areas. Examples of such toolkits include elastix⁴⁴, Slicer3D⁴⁵, ANTsX⁴⁶,
¹²³ and several others which have all been applied towards mouse brain spatial mapping. The
¹²⁴ main challenge, in these mouse-specific study scenarios, is that tailored pipelines often need
¹²⁵ be constructed from available software components. Investigators must therefore be familiar
¹²⁶ with the these tools for formulating new or adapting existing pipelines. However, in com-
¹²⁷ parison to previously described specialized mapping approaches, these approaches are often
¹²⁸ easier to create and prone to robustness, being typically constructed from pipelin compo-
¹²⁹ nents which have been previously vetted in other contexts. In this work, we highlight such
¹³⁰ mapping strategies designed using the ANTsX framework to map three distinct mouse cell
¹³¹ type data with different characteristics into existing CCFs.

¹³² **1.2 Advanced Normalization Tools (ANTsX)**

¹³³ The Advanced Normalization Tools Ecosystem (ANTsX) has been used in a number of
¹³⁴ applications for mapping mouse brain data as part of core processing steps in various
¹³⁵ workflows^{30,47–50}, particularly its pairwise, intensity-based image registration capabilities and
¹³⁶ bias field correction. Historically, ANTsX development is originally based on fundamental
¹³⁷ approaches to image mapping^{51–53}, particularly in the human brain, which has resulted
¹³⁸ in core contributions to the field such as the widely-used Symmetric Normalization (SyN)
¹³⁹ algorithm⁵⁴. Since its development, various independent platforms have been used to eval-
¹⁴⁰ uate ANTsX image registration capabilities in the context of different application foci which
¹⁴¹ include multi-site brain MRI data⁵⁵, pulmonary CT data⁵⁶, and most recently, multi-modal
¹⁴² brain registration in the presence of tumors⁵⁷.

¹⁴³ Apart from its registration capabilities, ANTsX comprises additional functionality such
¹⁴⁴ as template generation⁵⁸, intensity-based segmentation⁵⁹, preprocessing^{60,61}, deep learning
¹⁴⁵ networks⁴⁶, and other utilities relevant to brain mapping (see Table 1). The use of the toolkit
¹⁴⁶ has demonstrated high performance in multiple application areas (e.g., consensus labeling⁶²,
¹⁴⁷ brain tumor segmentation⁶³, and cardiac motion estimation⁶⁴). Importantly, ANTsX is built
¹⁴⁸ on the Insight Toolkit (ITK)⁶⁵ deriving benefit from the open-source community of sci-
¹⁴⁹ entists and programmers as well as providing an important resource for algorithmic develop-
¹⁵⁰ ment, evaluation, and improvement. In this paper we demonstrate how ANTsX provides a
¹⁵¹ comprehensive toolset provides the basis to develop modular frameworks for mapping di-
¹⁵² verse mouse cell type data into common coordinate frameworks (CCFs). Specifically, we
¹⁵³ highlight its application for mapping data from three separate BICCN projects focused on
¹⁵⁴ distinct data types: morphology data using fluorescence micro-optical sectioning tomog-
¹⁵⁵ raphy (fMOST), spatial transcriptomics from multiplexed error-robust fluorescence in situ
¹⁵⁶ hybridization (MERFISH) data, and time-series developmental data using light sheet fluores-
¹⁵⁷ cence microscopy (LSFM) and magnetic resonance imaging (MRI). We describe both shared
¹⁵⁸ and targeted strategies developed to address the specific challenges of these modalities.

¹⁵⁹ **1.3 Novel ANTsX-based open-source contributions**

¹⁶⁰ We introduce two novel inclusions to the ANTsX toolset that were developed as part of
¹⁶¹ the MRI mapping and analysis pipeline for the Developmental Common Coordinate Frame-
¹⁶² work (DevCCF). Consistent with previous ANTsX development, newly introduced capa-
¹⁶³ bilities introduced below are available through ANTsX (specifically, via R and Python
¹⁶⁴ ANTsX packages), and illustrated through self-contained examples in the ANTsX tuto-
¹⁶⁵ rial (<https://tinyurl.com/antsxtutorial>) with a dedicated GitHub repository specific to this
¹⁶⁶ work (<https://github.com/ntustison/ANTsXMouseBrainMapping>). To complement stan-
¹⁶⁷ dard preprocessing steps (e.g., bias correction, brain masking), additional mouse brain spe-
¹⁶⁸ cific tools have also been introduced to the ANTsX ecosystem, such as section reconstruction
¹⁶⁹ and landmark-based alignment with corresponding processing scripts (<https://github.com/>
¹⁷⁰ [dontminchenit/CCFAAlignmentToolkit](https://github.com/dontminchenit/CCFAAlignmentToolkit)).

¹⁷¹ **1.3.1 Continuously mapping the DevCCF detjectory with a velocity flow**
¹⁷² **model**

¹⁷³ Recently, the Developmental Common Coordinate Framework (DevCCF) was introduced to
¹⁷⁴ the mouse brain research community as a public resource¹⁶ comprising symmetric atlases of
¹⁷⁵ multimodal image data and anatomical segmentations defined by developmental ontology.
¹⁷⁶ These templates sample the mouse embryonic days E11.5, E13.5, E15.5, E18.5 and postna-
¹⁷⁷ tal days P4, P14, and P56. Modalities include light sheet floourescence miscroscopy (LSFM)
¹⁷⁸ and at least four MRI contrasts per developmental stage. Anatomical parcellations are also
¹⁷⁹ available for each time point and were generated from ANTsX-based mappings of gene ex-
¹⁸⁰ pression and other cell type data. Additionally, the P56 template was integrated with the
¹⁸¹ AllenCCFv3 to further enhance the practical utility of the DevCCF. These processes, specif-
¹⁸² ically template generation and multi-modal image mapping, were performed using ANTsX
¹⁸³ functionality in the presence of image mapping difficulties such as missing data and tissue
¹⁸⁴ distortion.

¹⁸⁵ Given the temporal gaps in the discrete set of developmental atlases, we also provide an

¹⁸⁶ open-source framework for inferring correspondence within the temporally continuous do-
¹⁸⁷ main sampled by the existing set of embryonic and postnatal atlases of the DevCCF. This
¹⁸⁸ recently developed functionality permits the generation of a diffeomorphic velocity flow trans-
¹⁸⁹ formation model⁶⁶, influenced by previous work⁶⁷. The resulting time-parameterized veloc-
¹⁹⁰ ity field spans the stages of the DevCCF where mappings between any two continuous time
¹⁹¹ points within the span bounded by the E11.5 and P56 atlases is determined by integration
¹⁹² of the optimized velocity field.

¹⁹³ 1.3.2 Automated structural parcellations of the mouse brain

¹⁹⁴ In contrast to the pipeline development in human data⁴⁶, limited tools exist yet to cre-
¹⁹⁵ ate adequate training data for automated parcellations of the mouse brain. In addition,
¹⁹⁶ mouse brain data acquisition often has unique issues, such as lower data quality or sampling
¹⁹⁷ anisotropy which limits its applicability to high resolution resources (e.g., AllenCCFv3, De-
¹⁹⁸ vCCF), specifically with respect to the corresponding granular brain parcellations derived
¹⁹⁹ from numerous hours of expert annotation leveraging multimodal imaging resources.

²⁰⁰ Herein, we introduce a mouse brain parcellation pipeline for T2-weighted (T2-w) MRI com-
²⁰¹ prising two novel deep learning components: two-shot learning brain extraction from data
²⁰² augmentation of two ANTsX templates generated from two open datasets^{68,69} and single-
²⁰³ shot brain parcellation derived from the AllenCCFv3 labelings mapped to the corresponding
²⁰⁴ DevCCF P56 T2-w component. Although we anticipate that this pipeline will be benefi-
²⁰⁵ cial to the research community, this work demonstrates more generally how one can leverage
²⁰⁶ ANTsX tools for developing quantitative mouse brain morphological tools using only publicly
²⁰⁷ available resources. Evaluation is performed on an independent open dataset⁷⁰ comprising
²⁰⁸ longitudinal acquisitions of multiple specimens.

209 **2 Results**

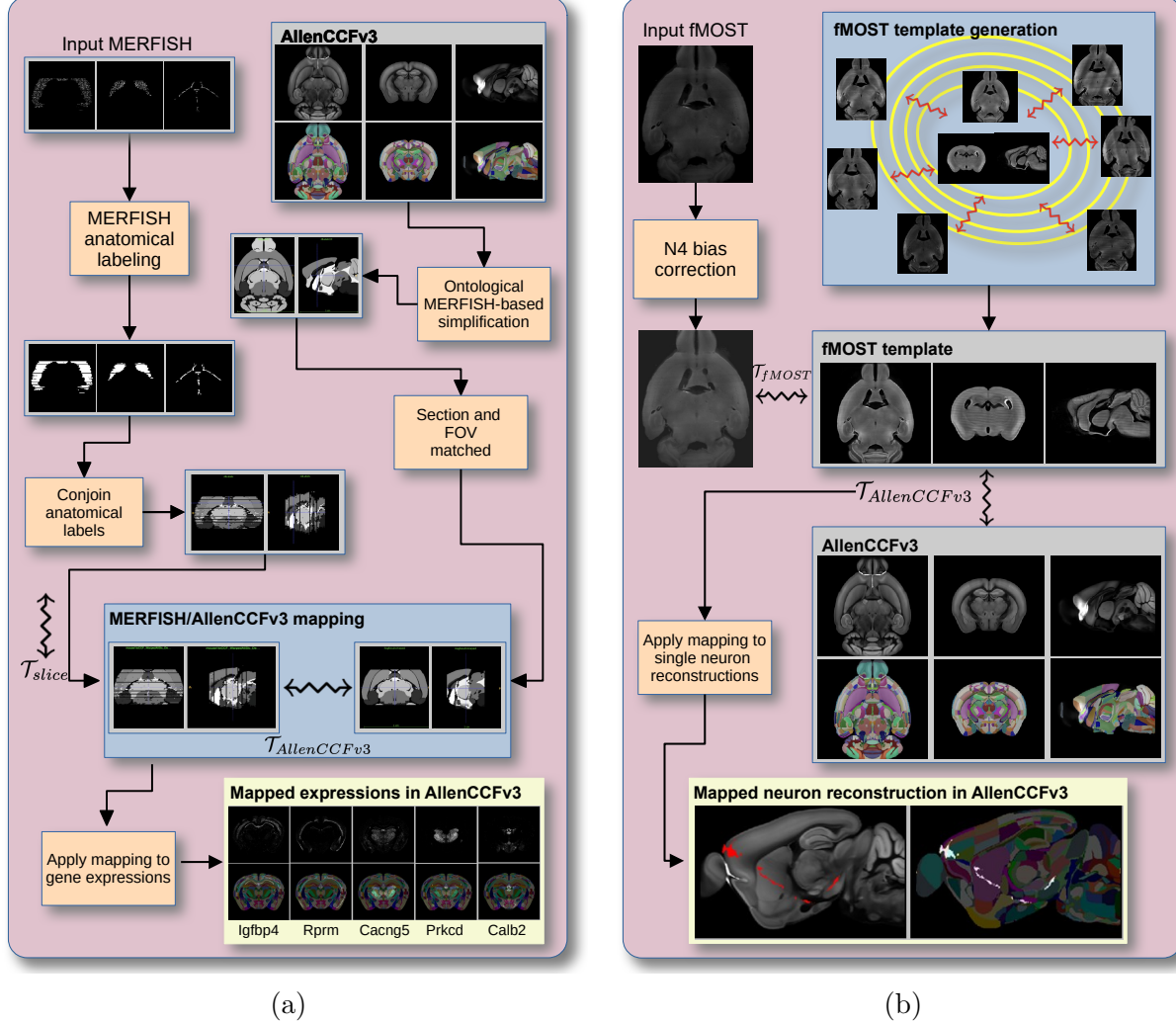


Figure 1: Diagram of the two ANTsX-based pipelines for mapping (a) MERFISH and (b)fMOST data into the space of AllenCCFv3. Each generates the requisite transforms, \mathcal{T} , to map individual images.

210 **2.1 AllenCCFv3 brain image mapping**

211 **2.1.1 Mapping multiplexed error-robust fluorescence *in situ* hybridization
212 (MERFISH) data**

213 **Overview.** The ANTsX framework was used to develop a pipeline for mapping multiplexed
214 error-robust fluorescence *in situ* hybridization (MERFISH) spatial transcriptomic mouse

215 data onto the AllenCCFv3 (see Figure 1(a)). This pipeline, used recently in creating a
216 high-resolution transcriptomic atlas of the mouse brain⁵⁰, performs mappings by first gen-
217 erating anatomical labels from tissue related gene expressions in the MERFISH data, and
218 then spatially matching these labels to corresponding anatomical tissue parcellations in the
219 AllenCCFv3. The pipeline consists of MERFISH data specific preprocessing which includes
220 section reconstruction, mapping corresponding anatomical labels between AllenCCFv3 and
221 the spatial transcriptomic maps of the MERFISH data, and matching MERFISH sections to
222 the atlas space. Following pre-processing, two main alignment steps were performed: 1) 3-D
223 global affine mapping and section matching of the AllenCCFv3 into the MERFISH data and
224 2) 2D global and deformable mapping between each MERFISH section and matched AllenC-
225 CFv3 section. Mappings learned via each step in the pipeline are preserved and concatenated
226 to provide point-to-point correspondence between the original MERFISH data and AllenC-
227 CFv3, thus allowing individual gene expressions to be transferred into the AllenCCFv3.

228 **Data.** MERFISH mouse brain data was acquired using a previously detailed procedure⁵⁰.
229 Briefly, a brain of C57BL/6 mouse was dissected according to standard procedures and
230 placed into an optimal cutting temperature (OCT) compound (Sakura FineTek 4583) in
231 which it was stored at -80°C. The fresh frozen brain was sectioned at 10 μ m on Leica 3050
232 S cryostats at intervals of 200 μ m to evenly cover the brain. A set of 500 genes were imaged
233 that had been carefully chosen to distinguish the ~5200 clusters of our existing RNAseq
234 taxonomy. For staining the tissue with MERFISH probes, a modified version of instructions
235 provided by the manufacturer was used⁵⁰. Raw MERSCOPE data were decoded using
236 Vizgen software (v231). Cells were segmented based on DAPI and PolyT staining using
237 Cellpose^{71,72}. Segmentation was performed on a median z-plane (fourth out of seven) and
238 cell borders were propagated to z-planes above and below. To assign cluster identity to each
239 cell in the MERFISH dataset, we mapped the MERFISH cells to the scRNA-seq reference
240 taxonomy.

241 **Evaluation.** Alignment of the MERFISH data into the AllenCCFv3 was qualitatively as-
242 sessed by an expert anatomist at each iteration of the registration using known correspon-
243 dence of gene markers and their associations with the AllenCCFv3. As previously reported⁵⁰,

²⁴⁴ further assessment of the alignment showed that, of the 554 terminal regions (gray matter
²⁴⁵ only) in the AllenCCFv3, only seven small subregions were missed from the MERFISH
²⁴⁶ dataset: frontal pole, layer 1 (FRP1), FRP2/3, FRP5; accessory olfactory bulb, glomerular
²⁴⁷ layer (AOBgl); accessory olfactory bulb, granular layer (AOBgr); accessory olfactory bulb,
²⁴⁸ mitral layer (AOBmi); and accessory supraoptic group (ASO).

²⁴⁹ 2.1.2 Mapping fluorescence micro-optical sectioning tomography (fMOST) data

²⁵⁰ **Overview.** We developed a pipeline for mapping fluorescence micro-optical sectioning to-
²⁵¹ mography (fMOST) mouse brain images into the AllenCCFv3 (see Figure 1(b)). The pipeline
²⁵² is adapted from previously developed frameworks for human brain mapping⁵⁸, and uses a
²⁵³ modality specific (fMOST) average atlas to assist in the image registration and mapping.
²⁵⁴ This approach has been well validated in human studies^{73–75}, and successfully used in other
²⁵⁵ mouse data^{12,15,34}. Briefly, we construct an intensity- and shape-based average fMOST atlas
²⁵⁶ using 30 fMOST images to serve as an intermediate registration target for mapping fMOST
²⁵⁷ images from individual specimens into the AllenCCFv3. Preprocessing steps include down-
²⁵⁸ sampling to match the 25 μ m isotropic AllenCCFv3, acquisition-based stripe artifact removal,
²⁵⁹ and inhomogeneity correction⁶¹. Preprocessing also includes a single annotation-driven reg-
²⁶⁰ istration to establish a canonical mapping between the fMOST atlas and the AllenCCFv3.
²⁶¹ This step allows us to align expert determined landmarks to accurately map structures
²⁶² with large morphological differences between the modalities, which are difficult to address
²⁶³ using standard approaches. Once this canonical mapping is established, standard intensity-
²⁶⁴ based registration is used to align each new fMOST image to the fMOST specific atlas.
²⁶⁵ This mapping is concatenated with the canonical fMOST atlas-to-AllenCCFv3 mapping to
²⁶⁶ further map each individual brain into the latter without the need to generate additional
²⁶⁷ landmarks. Transformations learned through this mapping can be applied to single neuron
²⁶⁸ reconstructions from the fMOST images to evaluate neuronal distributions across different
²⁶⁹ specimens into the AllenCCFv3 for the purpose of cell census analyses.

²⁷⁰ **Data.** The high-throughput and high-resolution fluorescence micro-optical sectioning to-
²⁷¹ mography (fMOST)^{76,77} platform was used to image 55 mouse brains containing gene-defined

neuron populations, with sparse transgenic expression^{78,79}. In short, the fMOST imaging platform results in 3-D images with voxel sizes of $0.35 \times 0.35 \times 1.0 \mu\text{m}^3$ and is a two-channel imaging system where the green channel displays the green fluorescent protein (GFP) labeled neuron morphology and the red channel is used to visualize the counterstained propidium iodide cytoarchitecture. The spatial normalizations described in this work were performed using the red channel, which offered higher tissue contrast for alignment, although other approaches are possible including multi-channel registration.

Evaluation. Evaluation of the canonical fMOST atlas to Allen CCFv3 mapping was performed via quantitative comparison at each step of the registration and qualitative assessment of structural correspondence after alignment by an expert anatomist. Dice values were generated for the following structures: whole brain, 0.99; fimbria, 0.91; habenular commissure, 0.63; posterior choroid plexus, 0.93; anterior choroid plexus, 0.96; optic chiasm, 0.77; caudate putamen, 0.97. Similar qualitative assessment was performed for each fMOST specimen including the corresponding neuron reconstruction data.

2.2 Continuously mapping the DevCCF trajectory with a velocity flow model

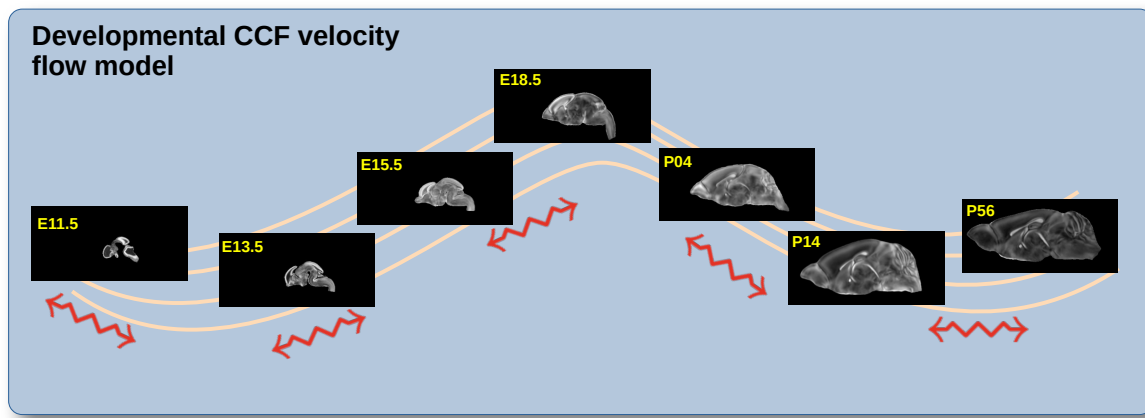


Figure 2: The spatial transformation between any two time points within the continuous DevCCF longitudinal developmental trajectory is available through the use of ANTsX functionality for generating a velocity flow model.

288 The DevCCF is an openly accessible resource for the mouse brain research community¹⁶. It
289 consists of multi-modal MRI and LSFM symmetric ANTsX-generated templates⁵⁸ sampling
290 the mouse brain developmental trajectory, specifically the embryonic (E) and postnatal (P)
291 days E11.5, E13.5, E15.5, E18.5 P4, P14, and P56. Each template space includes structural
292 labels defined by a developmental ontology. Its utility is also enhanced by a coordinated
293 construction with AllenCCFv3. Although this work represents a significant contribution, the
294 gaps between timepoints potentially limit its applicability which could be addressed through
295 the development of the ability to map not only between timepoints but also within and
296 across timepoints.

297 To continuously generate transformations between the different stages of the DevCCF atlases,
298 we developed a general velocity flow model approach which we apply to DevCCF-derived
299 data. We also introduce this functionality into both the ANTsR and ANTsPy packages (for
300 the latter, see `ants.fit_time_varying_transform_to_point_sets(...)`) for potential
301 application to this and other analogous scenarios (e.g., modeling the cardiac and respiratory
302 cycles). ANTsX, being built on top of ITK, uses an ITK image data structure for the 4-D
303 velocity field where each voxel contains the x , y , z components of the field at that point.

304 2.2.1 Data

305 Labeled annotations are available as part of the original DevCCF and reside in the space
306 of each developmental template which range in resolution from $31.5 - 50\mu\text{m}$. Across all
307 atlases, the total number of labeled regions exceeds 2500. From these labels, a common set
308 of 26 labels (13 per hemisphere) across all atlases were used for optimization and evaluation.
309 These simplified regions include: terminal hypothalamus, subpallium, pallium, peduncular
310 hypothalamus, prosomere, prosomere, prosomere, midbrain, prepontine hindbrain, pontine
311 hindbrain, pontomedullary hindbrain, medullary hindbrain, and tracts (see Figure 3).

312 Prior to velocity field optimization, all data were rigidly transformed to DevCCF P56 using
313 the centroids of the common label sets. In order to determine the landmark correspondence
314 across DevCCF stages, the multi-metric capabilities of `ants.registration(...)` were used.
315 Instead of performing intensity-based pairwise registration directly on these multi-label im-

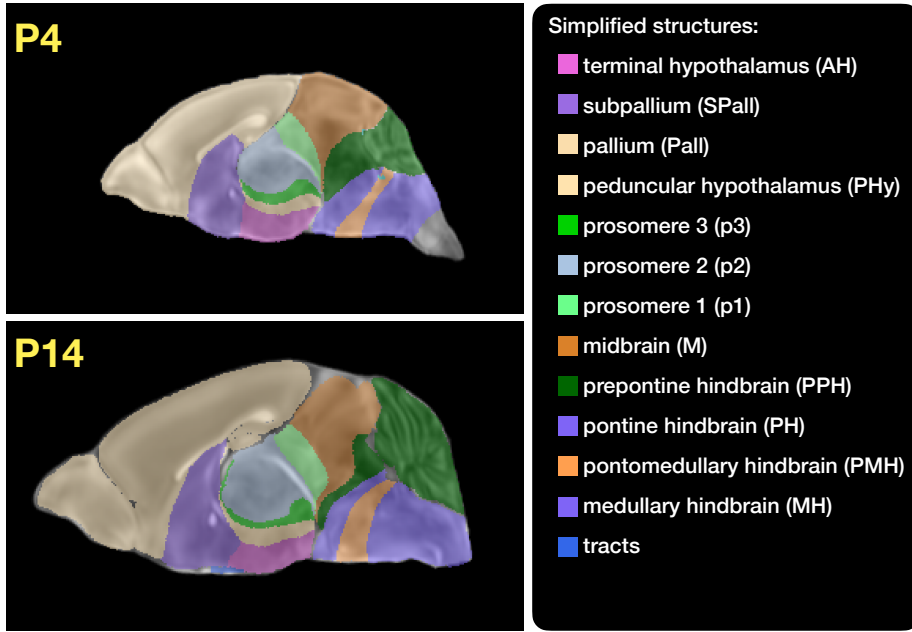


Figure 3: Annotated regions representing common labels across developmental stages which are illustrated for both P4 and P14.

316 ages, each label was used to construct a separate fixed and moving image pair resulting in a
 317 multi-metric registration optimization scenario involving 24 binary image pairs (each label
 318 weighted equally) for optimizing diffeomorphic correspondence between neighboring time
 319 point atlases using the mean squares metric and the symmetric normalization transform⁵⁴.

320 To generate the set of common point sets across all seven developmental atlases, the label
 321 boundaries and whole regions were sampled in the P56 atlas and then propagated to each
 322 atlas using the transformations derived from the pairwise registrations. We selected a sam-
 323 pling rate of 10% for the contour points and 1% for the regional points for a total number
 324 of points being per atlas being 173303 ($N_{contour} = 98151$ and $N_{region} = 75152$). Regional
 325 boundary points were weighted twice as those of non-boundary points during optimization.

326 2.2.2 Optimization

327 The velocity field was optimized using the input composed of the seven corresponding point
 328 sets and their associated weight values, the selected number of integration points for the
 329 velocity field ($N = 11$), and the parameters defining the geometry of the spatial dimensions

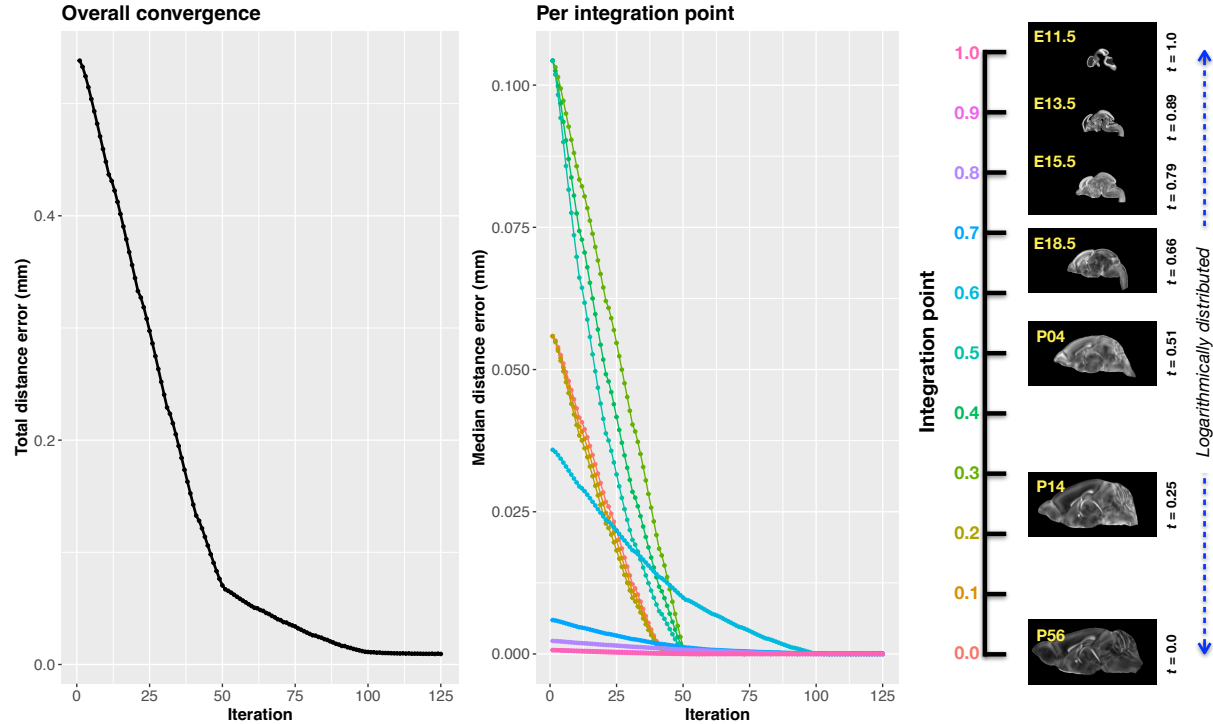


Figure 4: Convergence of the optimization of the velocity field for describing the transformation through the developmental stages from E11.5 through P56. Integration points in diagram on the right are color-coordinated with the center plot and placed in relation to the logarithmically situated temporal placement of the individual DevCCF atlases.

330 of the velocity field. Thus, the optimized velocity field described here is of size [256, 182, 360]
 331 (50 μ m isotropic) \times 11 integration points for a total compressed size of a little over 2 GB.
 332 This choice represented weighing the trade-off between tractability, portability, and accuracy.
 333 However, all data and code to reproduce the results described (with possible variation in the
 334 input parameters) are available in the dedicated GitHub repository.

335 The normalized time point scalar value for each atlas/point-set in the temporal domains [0, 1]
 336 was also defined. Given the increasingly larger gaps in the postnatal timepoint sampling, we
 337 made two adjustments. Based on known mouse brain development, we used 28 days for the
 338 P56 data. We then computed the log transform of the adjusted set of time points prior to
 339 normalization between 0 and 1 (see the right side of Figure 4). This log transform, as part
 340 of the temporal normalization, significantly improved data spacing.

341 The maximum number of iterations was set to 200 with each iteration taking approximately
 342 six minutes on a 2020 iMac (processor, 3.6 GHz 10-Core Intel Core i9; memory, 64 GB 2667

343 MHz DDR4) At each iteration we looped over the 11 integration points. At each integration
 344 point, the velocity field estimate was updated by warping the two immediately adjacent
 345 point sets to the integration time point and determining the regularized displacement field
 346 between the two warped point sets. As with any gradient-based descent algorithm, this field
 347 was multiplied by a small step size ($\delta = 0.2$) before adding to the current velocity field.
 348 Convergence is determined by the average displacement error over each of the integration
 349 points. As can be seen in the left panel of Figure 4, convergence occurred around 125
 350 iterations when the average displacement error over all integration points is minimized. The
 351 median displacement error at each of the integration points also trends towards zero but at
 352 different rates.

353 2.2.3 The transformation model

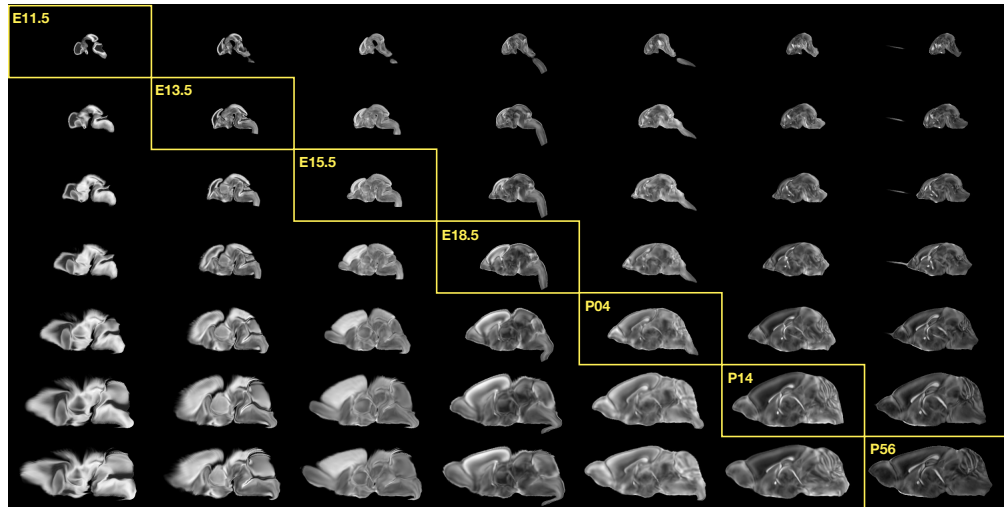


Figure 5: Mid-sagittal visualization of the effects of the transformation model in warping every developmental stage to the time point of every other developmental stage. The original images are located along the diagonal. Columns correspond to the warped original image whereas the rows represent the reference space to which each image is warped.

354 Once optimized, the resulting velocity field can be used to generate the deformable transform
 355 between any two continuous points within the time interval bounded by E11.5 and P56. As
 356 a demonstration, in Figure 5, we transform each atlas to the space of every other atlas
 357 using the DevCCF transform model. Additionally, one can use this transformation model
 358 to construct virtual templates in the temporal gaps of the DevCCF. Given an arbitrarily

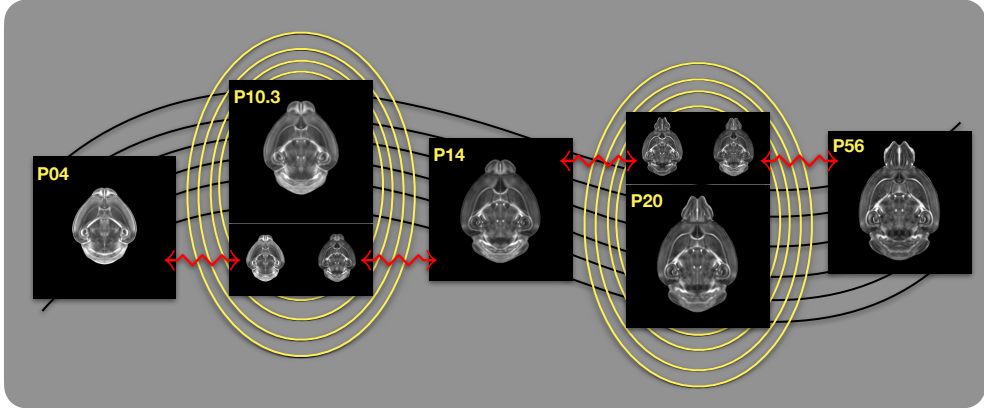


Figure 6: Illustration of the use of the velocity flow model for creating virtual templates at continuous time points not represented in one of the existing DevCCF time points. For example, FA templates at time point P10.3 and P20 can be generated by warping the existing temporally adjacent developmental templates to the target time point and using those images in the ANTsX template building process.

359 chosen time point within the normalized time point interval, the existing adjacent DevCCF
 360 atlases on either chronological side can be warped to the desired time point. A subsequent
 361 call to one of the ANTsX template building functions then permits the construction of the
 362 template at that time point. In Figure 6, we illustrate the use of the DevCCF velocity flow
 363 model for generating two such virtual templates for two arbitrary time points. Note that
 364 both of these usage examples can be found in the GitHub repository previously given.

365 2.3 Automated structural parcellations of the mouse brain

366 Brain parcellation strategies for the mouse brain are pivotal for understanding the complex
 367 organization and function of murine nervous system⁸⁰. By dividing the brain into distinct
 368 regions based on anatomical, physiological, or functional characteristics, researchers can
 369 investigate specific areas in isolation and identify their roles in various behaviors and pro-
 370 cesses. For example, such parcellation schemes can help elucidate the spatial distribution of
 371 gene expression patterns⁸¹ as well as identify functional regions involved in specific cognitive
 372 tasks⁸².

373 Although deep learning techniques have been used to develop useful parcellation tools for
 374 human brain research (e.g., SynthSeg⁸³, ANTsXNet⁴⁶), analogous development for the mouse

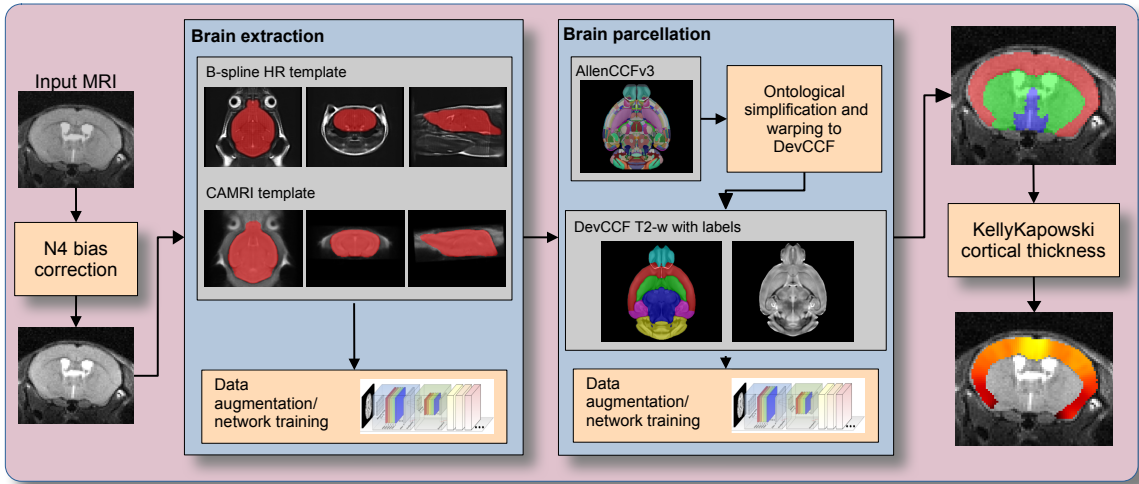


Figure 7: The mouse brain cortical parcellation pipeline integrating two deep learning components for brain extraction and brain parcellation prior to estimating cortical labels. Both deep learning networks rely heavily on aggressive data augmentation on templates built from open data and provide an outline for further refinement and creating alternative parcellations for tailored research objectives. Possible applications include measurement of voxelwise cortical thickness measurements.

375 brain is limited. In addition, mouse data is often characterized by unique imaging issues such
 376 as extreme anisotropic sampling which are often in sharp contrast to the high resolution
 377 template-based resources available within the community, e.g., AllenCCFv3 and DevCCF.
 378 We demonstrate how one can use the ANTsX tools to develop a complete mouse brain
 379 structural morphology pipeline as illustrated in Figure 7 and detailed below.

380 2.3.1 Two-shot mouse brain extraction network

381 In order to create a generalized mouse brain extraction network, we built whole-head tem-
 382 plates from two publicly available datasets. The Center for Animal MRI (CAMRI) dataset⁶⁸
 383 from the University of North Carolina at Chapel Hill consists of 16 T2-w MRI volumes of
 384 voxel resolution $0.16 \times 0.16 \times 0.16 mm^3$. The second high-resolution dataset⁶⁹ comprises
 385 88 specimens each with three spatially aligned canonical views with in-plane resolution of
 386 $0.08 \times 0.08 mm^2$ with a slice thickness of $0.5 mm$. These three orthogonal views were used
 387 to reconstruct a single high-resolution volume per subject using a B-spline fitting algorithm
 388 available in ANTsX⁸⁴. From these two datasets, two symmetric isotropic ANTsX templates⁵⁸

³⁸⁹ were generated analogous to the publicly available ANTsX human brain templates used in
³⁹⁰ previous research⁸⁵. Bias field simulation, intensity histogram warping, noise simulation,
³⁹¹ random translation and warping, and random anisotropic resampling in the three canonical
³⁹² directions were used for data augmentation in training a T2-w brain extraction network.

³⁹³ 2.3.2 Single-shot mouse brain parcellation network

³⁹⁴ AllenCCFv3 and its hierarchical ontological labeling, along with the DevCCF, provides the
³⁹⁵ necessary data for developing a tailored structural parcellation network for multimodal imag-
³⁹⁶ ing. The `allensdk` Python library permits the creation of any gross parcellation based on the
³⁹⁷ AllenCCFv3 ontology. For example, using `allensdk` we coalesced the labels to the following
³⁹⁸ six major structures: cerebral cortex, cerebral nuclei, brain stem, cerebellum, main olfac-
³⁹⁹ tory bulb, and hippocampal formation. This labeling was mapped to the P56 component
⁴⁰⁰ of the DevCCF for use with the T2-w template component. Both the T2-w P56 DevCCF
⁴⁰¹ and labelings, in conjunction with the data augmentation described previously for brain ex-
⁴⁰² traction, were used to train the proposed brain parcellation network. Note that other brain
⁴⁰³ parcellation networks have also been made available in the same ANTsXNet functionality
⁴⁰⁴ using other regions and modalities.

⁴⁰⁵ 2.3.3 Evaluation

⁴⁰⁶ Although the utility of the proposed brain parcellation framework is highly dependent on the
⁴⁰⁷ specific application, we demonstrate the utility through the generation of cortical thickness
⁴⁰⁸ maps⁸⁶ which leverages both brain parcellation and the capabilities of mouse brain-based
⁴⁰⁹ isotropic interpolation for anisotropic data. Cortical thickness has demonstrated utility in
⁴¹⁰ both human (e.g.,^{85,87}) and non-human data (e.g., canines⁸⁸, dolphins⁸⁹, non-human primates
⁴¹¹ [^{90;@}]) including the mouse brain^{41,91–93}.

⁴¹² For evaluation, we used an additional publicly available dataset⁷⁰ which is completely inde-
⁴¹³ pendent from the data used in training the brain extraction and parcellation networks. Data
⁴¹⁴ includes 12 specimens each imaged at seven time points (Day 0, Day 3, Week 1, Week 4, Week

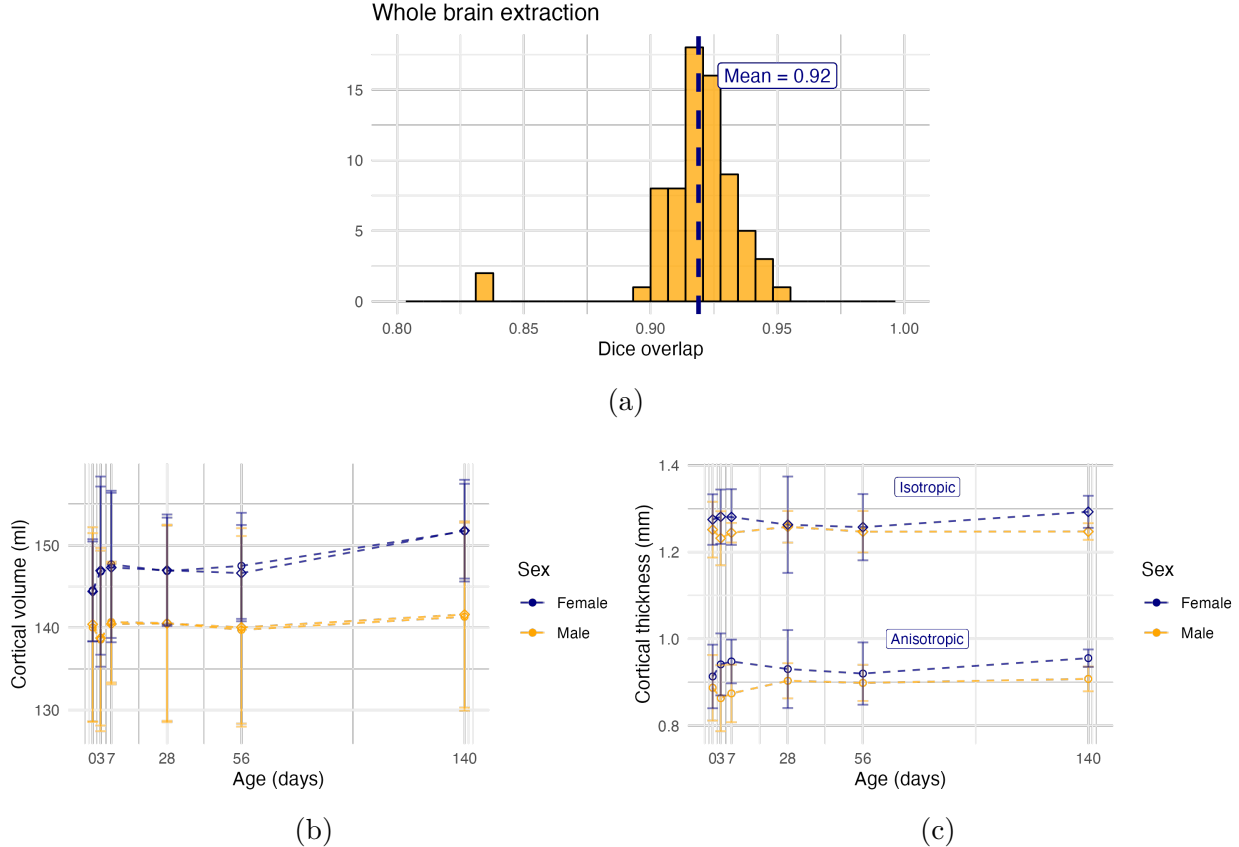


Figure 8: Evaluation of the ANTsX mouse brain extraction, parcellation, and cortical thickness pipeline on an independent dataset consisting of 12 specimens \times 7 time points = 84 total images. (a) Dice overlap comparisons with the user-generated brain masks provide good agreement with the automated results from the brain extraction network. (b) Cortical volume measurements show similar average quantities over growth and development between the original anisotropic data and interpolated isotropic data. (c) The volumetric comparative results contrast with the cortical thickness measurements which illustrate estimation in anisotropic space severely underestimates the actual values in comparison with the isotropic prediction.

415 8, Week 20) with in-house-generated brain masks. Spacing is anisotropic with an in-plane
416 resolution of $0.1 \times 0.1 mm^2$ and a slice thickness of $0.5 mm$. Since the training data is isotropic
417 and data augmentation includes downsampling in the canonical directions, each of the two
418 networks learns mouse brain-specific interpolation such that one can perform prediction on
419 thick-sliced images, as, for example, in these evaluation data, and return isotropic probabil-
420 ity and thickness maps (a choice available to the user). Figure 8 summarizes the results of
421 the evaluation and comparison between isotropic and anisotropic cortical measurements in
422 male and female specimens.

423 **3 Discussion**

424 The diverse mouse brain cell type profiles gathered through BICCN and associated efforts
425 provides a rich multi-modal resource to the research community. However, despite significant
426 progress, optimized leveraging of these valuable resources is ongoing. A central component
427 to data integration is accurately mapping novel cell type data to into common coordinate
428 frameworks (CCFs) for subsequent processing and analysis. To meet these needs, tools
429 for mapping mouse cell type data must be both generally accessible to a wide audience
430 of investigators, and capable of handling distinct challenges unique to each data type. In
431 this work, we described modular ANTsX-based pipelines developed to address the needs of
432 three BICCN projects that cover distinct cell type data, including spatial transcriptomic,
433 morphological, and developmental data. We highlighted how a modular toolbox like ANTsX
434 can be tailored to address problems unique to each modality through leveraging a variety
435 of ready-to-use powerful tools that have been previously validated in multiple application
436 scenarios.

437 Our MERFISH pipeline provides an example of how to map high-resolution spatial transcrip-
438 tomic data into the AllenCCFv3. While the techniques employed for mapping the sectioned
439 data can be generally applicable to spatially transform other serial histology images, much
440 of the pipeline was designed to specifically address known alignment challenges in the MER-
441 FISH data. Thus pipeline shows how general ANTsX tools can be adapted to target highly
442 specialized problems in mouse cell type data.

443 In contrast to the MERFISH pipeline, our fMOST pipeline was designed to be a more general
444 solution that can be employed in other modalities. The pipeline primarily uses previously
445 developed ANTsX preprocessing and atlasing tools to map fMOST data into the AllenCCFv3.
446 The key component of the pipeline is the use of a fMOST-specific average shape and intensity
447 atlas to most effectively address image registration in this context. The mapping between
448 the fMOST atlas is generated once and reused for each new fMOST image. Lastly, ANTsX
449 provides point set transformation tools to allow the mappings found through the pipeline to
450 be directly applied to associated single-cell reconstructions from the fMOST data to study
451 neuronal morphology.

452 The pipeline for continuously mapping the DevCCF data is also available in ANTsX and
453 is generally applicable for spatio-temporal mapping. With specific application to the De-
454 vCCF, despite the significant expansion of available developmental age templates beyond
455 what existed previously, there are still temporal gaps in the DevCCF which can be poten-
456 tially sampled by future research efforts. However, pioneering work involving time-varying
457 diffeomorphic transformations allow us to continuously situate the existing templates within
458 a velocity flow model. This allows one to determine the diffeomorphic transformation from
459 any one temporal location to any other temporal location within the time span defined by
460 the temporal limits of the DevCCF. This functionality is built on multiple ITK components
461 including the B-spline scattered data approximation technique for field regularization and
462 velocity field integration. This velocity field model permits intra-template comparison and
463 the construction of virtual templates where a template can be estimated at any continuous
464 time point within the temporal domain. This novel application can potentially enhance our
465 understanding of intermediate developmental stages.

466 We also presented a mouse brain morphological pipeline for brain extraction and brain
467 parcellation using single-shot and two-shot learning with data augmentation. This approach
468 attempts to circumvent (or at least minimize) the typical requirement of large training
469 datasets as with the human ANTsX pipeline analog. However, even given our initial success
470 on independent data, we anticipate that refinements will be necessary. Given that the ANTsX
471 toolkit is a dynamic effort undergoing continual improvement, we manually correct cases that
472 fail and use them for future training and refinement of network weights as we have done for
473 our human-based networks. Generally, these approaches provide a way to bootstrap training
474 data for manual refinement and future generation of more accurate deep learning networks
475 in the absence of other applicable tools.

476 The ANTsX ecosystem is a powerful framework that has demonstrated applicability to di-
477 verse cell type data in the mouse brain. This is further evidenced by the many software
478 packages that use various ANTsX components in their own mouse-specific workflows. The
479 extensive functionality of ANTsX makes it possible to create complete processing pipelines
480 without requiring the integration of multiple packages or lengthy software development.

- ⁴⁸¹ These open-source components not only perform well but are available across multiple plat-
⁴⁸² forms which facilitates the construction of tailored pipelines for individual study solutions.
⁴⁸³ These components are also supported by years of development not only by the ANTsX
⁴⁸⁴ development team but by the larger ITK community.

485 **4 Methods**

486 The following methods are all available as part of the ANTsX ecosystem with analogous
487 elements existing in both ANTsR (ANTs in R) and ANTsPy (ANTs in Python) with an
488 ANTs/ITK C++ core. However, most of the development for the work described below was
489 performed using ANTsPy. For equivalent calls in ANTsR, please see the ANTsX tutorial at
490 <https://tinyurl.com/antsxtutorial>.

491 **4.1 General ANTsX utilities**

492 Although they focus on distinct data types, the three pipelines presented share common
493 components that are generally applicable when mapping mouse cell type data. These include,
494 addressing intensity biases and noise in the data, image registration to solve the mapping,
495 creating custom templates and atlases from the data, and visualization of the results. Table
496 1 provides a brief summary of key general functionalities in ANTsX for addressing these
497 challenges.

498 **4.1.1 Preprocessing: bias field correction and denoising**

499 Bias field correction and image denoising are standard preprocessing steps in improving over-
500 all image quality in mouse brain images. The bias field, a gradual spatial intensity variation
501 in images, can arise from various sources such as magnetic field inhomogeneity or acquisition
502 artifacts, leading to distortions that can compromise the quality of brain images. Correct-
503 ing for bias fields ensures a more uniform and consistent representation of brain structures,
504 enabling more accurate quantitative analysis. Additionally, brain images are often suscep-
505 tible to various forms of noise, which can obscure subtle features and affect the precision
506 of measurements. Denoising techniques help mitigate the impact of noise, enhancing the
507 signal-to-noise ratio and improving the overall image quality. The well-known N4 bias field
508 correction algorithm⁶¹ has its origins in the ANTs toolkit which was implemented and intro-
509 duced into the ITK toolkit, i.e. `ants.n4_bias_field_correction(...)`. Similarly, ANTsX

Table 1: Sampling of ANTsX functionality

<i>ANTsPy: Preprocessing</i>	
bias field correction	<code>n4_bias_field_correction(...)</code>
image denoising	<code>denoise_image(...)</code>
<i>ANTsPy: Registration</i>	
image registration	<code>registration(...)</code>
image transformation	<code>apply_transforms(...)</code>
template generation	<code>build_template(...)</code>
landmark registration	<code>fit_transform_to_paired_points(...)</code>
time-varying landmark reg.	<code>fit_time_varying_transform_to_point_sets(...)</code>
integrate velocity field	<code>integrate_velocity_field(...)</code>
invert displacement field	<code>invert_displacement_field(...)</code>
<i>ANTsPy: Segmentation</i>	
MRF-based segmentation	<code>atropos(...)</code>
Joint label fusion	<code>joint_label_fusion(...)</code>
diffeomorphic thickness	<code>kelly_kapowski(...)</code>
<i>ANTsPy: Miscellaneous</i>	
Regional intensity statistics	<code>label_stats(...)</code>
Regional shape measures	<code>label_geometry_measures(...)</code>
B-spline approximation	<code>fit_bspline_object_to_scattered_data(...)</code>
Visualize images and overlays	<code>plot(...)</code>
<i>ANTsPyNet: Mouse-specific</i>	
brain extraction	<code>mouse_brain_extraction(...modality="t2"...)</code> <code>mouse_brain_extraction(...modality="ex5"...)</code>
brain parcellation	<code>mouse_brain_parcellation(...)</code>
cortical thickness	<code>mouse_cortical_thickness(...)</code>
super resolution	<code>mouse_histology_super_resolution(...)</code>

ANTsX provides state-of-the-art functionality for processing biomedical image data. Such tools, including deep learning networks, support a variety of mapping-related tasks. A more comprehensive listing of ANTsX tools with self-contained R and Python examples is provided as a gist page on GitHub (<https://tinyurl.com/antsxtutorial>).

510 contains an implementation of a well-performing patch-based denoising technique⁶⁰ and is
511 also available as an image filter to the ITK community, `ants.denoise_image(...)`.

512 4.1.2 Image registration

513 The ANTs registration toolkit is a complex framework permitting highly tailored solutions
514 to pairwise image registration scenarios⁹⁴. It includes innovative transformation models
515 for biological modeling^{54,67} and has proven capable of excellent performance^{55,95}. Vari-
516 ous parameter sets targeting specific applications have been packaged with the different
517 ANTsX packages, specifically ANTs, ANTsPy, and ANTsR⁴⁶. In ANTsPy, the function
518 `ants.registration(...)` is used to register a pair of images or a pair of image sets where
519 `type_of_transform` is a user-specified option that invokes a specific parameter set. For ex-
520 ample `type_of_transform='antsRegistrationSyNQuick[s]'` encapsulates an oft-used pa-
521 rameter set for quick registration whereas `type_of_transform='antsRegistrationSyN[s]'`
522 is a more aggressive alternative. Transforming images using the derived transforms is per-
523 formed via the `ants.apply_transforms(...)` function.

524 Initially, linear optimization is initialized with center of (intensity) mass alignment typically
525 followed by optimization of both rigid and affine transforms using the mutual information
526 similarity metric. This is followed by diffeomorphic deformable alignment using symmetric
527 normalization (SyN) with Gaussian⁵⁴ or B-spline regularization⁶⁷ where the forward trans-
528 form is invertible and differentiable. The similarity metric employed at this latter stage is
529 typically either neighborhood cross-correlation or mutual information. Note that these pa-
530 rameter sets are robust to input image type (e.g., light sheet fluorescence microscopy, Nissl
531 staining, and the various MRI modalities) and are adaptable to mouse image geometry and
532 scaling. Further details can be found in the various documentation sources for these ANTsX
533 packages.

534 4.1.3 Template generation

535 ANTsX provides functionality for constructing templates from a set (or multi-modal sets) of
536 input images as originally described⁵⁸ and recently used to create the DevCCF templates¹⁶.

537 An initial template estimate is constructed from an existing subject image or a voxelwise
538 average derived from a rigid pre-alignment of the image population. Pairwise registration
539 between each subject and the current template estimate is performed using the Symmetric
540 Normalization (SyN) algorithm⁵⁴. The template estimate is updated by warping all subjects
541 to the space of the template, performing a voxelwise average, and then performing a “shape
542 update” of this latter image by warping it by the average inverse deformation, thus yielding
543 a mean image of the population in terms of both intensity and shape. The corresponding
544 ANTsPy function is `ants.build_template(...)`.

545 **4.1.4 Visualization**

546 To complement the well-known visualization capabilities of R and Python, e.g., `ggplot2`
547 and `matplotlib`, respectively, image-specific visualization capabilities are available in the
548 `ants.plot(...)` function (Python). These are capable of illustrating multiple slices in
549 different orientations with other image overlays and label images.

550 **4.2 Mapping fMOST data to AllenCCFv3**

551 **4.2.1 Preprocessing**

- 552 • *Downsampling.* The first challenge when mapping fMOST images into the AllenCCFv3
553 is addressing the resolution scale of the data. Native fMOST data from an individual
554 specimen can range in the order of terabytes, which leads to two main problems. First,
555 volumetric registration methods (particularly those estimating local deformation) have
556 high computational complexity and typically cannot operate on such high-resolution
557 data under reasonable memory and runtime constraints. Second, the resolution of
558 the AllenCCFv3 atlas is much lower than the fMOST data, thus the mapping process
559 will cause much of the high-resolution information in the fMOST images to be lost
560 regardless. Thus, we perform a cubic B-spline downsampling of the fMOST data to
561 reduce the resolution of each image to match the isotropic $25 \mu\text{m}$ voxel resolution of the
562 AllenCCFv3 intensity atlas using `ants.resample_image(...)`. An important detail

563 to note is that while the fMOST images and atlas are downsampled, the mapping
564 learned during the registration is assumed to be continuous. Thus, after establishing
565 the mapping to the AllenCCFv3, we can interpolate the learned mapping and apply it
566 directly to the high-resolution native data directly to transform any spatially aligned
567 data (such as the single-cell neuron reconstructions) into the AllenCCFv3.

- 568 • *Stripe artifact removal.* Repetitive pattern artifacts are a common challenge in fMOST
569 imaging where inhomogeneity during the cutting and imaging of different sections can
570 leave stripes of hyper- and hypo-intensity across the image. These stripe artifacts
571 can be latched onto by the registration algorithm as unintended features that are
572 then misregistered to non-analogous structures in the AllenCCFv3. We address these
573 artifacts by fitting a 3-D bandstop (notch) filter to target the frequency of the stripe
574 patterns and removing them prior to the image registration.
- 575 • *Inhomogeneity correction.* Regional intensity inhomogeneity can also occur within
576 and between sections in fMOST imaging due to staining or lighting irregularity during
577 acquisition. Similar to stripe artifacts, intensity gradients due to inhomogeneity
578 can be misconstrued as features during the mapping and result in matching of non-
579 corresponding structures. Our pipeline addresses these intensity inhomogeneities using
580 N4 bias field correction⁶¹, `ants.n4_bias_field_correction(...)`.

581 4.2.2 Steps for spatial normalization to AllenCCFv3

- 582 1. *Average fMOST atlas as an intermediate target.* Due to the preparation of the mouse
583 brain for fMOST imaging, the resulting structure in the mouse brain has several large
584 morphological deviations from the AllenCCFv3 atlas. Most notable of these is an en-
585 largement of the ventricles, and compression of cortical structures. In addition, there is
586 poor intensity correspondence for the same anatomic features due to intensity dissim-
587 ilarity between imaging modalities. We have found that standard intensity-base reg-
588 istration is insufficient to capture the significant deformations required to map these
589 structures correctly into the AllenCCFv3. We address this challenge in ANTsX by
590 using explicitly corresponding parcellations of the brain, ventricles and surrounding

591 structures to directly recover these large morphological differences. However, generating
592 these parcellations for each individual mouse brain is a labor-intensive task. Our
593 solution is to create an average atlas whose mapping to AllenCCFv3 encapsulates these
594 large morphological differences to serve as an intermediate registration point. This has
595 the advantage of only needing to generate one set of corresponding annotations which
596 is used to register between the two atlas spaces. New images are first aligned to the
597 fMOST average atlas, which shares common intensity and morphological features and
598 thus can be achieved through standard intensity-based registration.

599 2. *Average fMOST atlas construction.* An intensity and shape-based contralaterally sym-
600 metric average of the fMOST image data is constructed from 30 images and their
601 contralateral flipped versions. We ran three iterations of the atlas construction using
602 the default settings. Additional iterations (up to six) were evaluated and showed mini-
603 mal changes to the final atlas construction, suggesting a convergence of the algorithm.

604 3. *fMOST atlas to AllenCCFv3 alignment.* Alignment between the fMOST average atlas
605 and AllenCCFv3 was performed using a one-time annotation-driven approach. Label-
606 to-label registration is used to align 7 corresponding annotations in both atlases in
607 the following: 1) brain mask/ventricles, 2) caudate/putamen, 3) fimbria, 4) posterior
608 choroid plexus, 5) optic chiasm, 6) anterior choroid plexus, and 7) habenular com-
609 missure. The alignments were performed sequentially, with the largest, most relevant
610 structures being aligned first using coarse registration parameters, followed by other
611 structures using finer parameters. This coarse-to-fine approach allows us to address
612 large morphological differences (such as brain shape and ventricle expansion) at the
613 start of registration and then progressively refine the mapping using the smaller struc-
614 tures. The overall ordering of these structures was determined manually by an expert
615 anatomist, where anatomical misregistration after each step of the registration was
616 evaluated and used to determine which structure should be used in the subsequent it-
617 eration to best improve the alignment. The transformation from this one-time expert-
618 guided alignment is preserved and used as the canonical fMOST atlas to AllenCCFv3
619 mapping in the pipeline.

- 620 4. *Alignment of individual fMOST mouse brains.* The canonical transformation between
621 the fMOST atlas and AllenCCFv3 greatly simplifies the registration of new individ-
622 ual fMOST mouse brains into the AllenCCFv3. Each new image is first registered
623 into the fMOST average atlas, which shares intensity, modality, and morphologi-
624 cal characteristics. This allows us to leverage standard, intensity-based registration
625 functionality⁹⁴ available in ANTsX to perform this alignment. Transformations are
626 then concatenated to the original fMOST image to move it into the AllenCCFv3 space
627 using `ants.apply_transforms(...)`.
- 628 5. *Transformation of single cell neurons.* A key feature of fMOST imaging is the ability
629 to reconstruct and examine whole-brain single neuron projections⁷⁹. Spatial mapping
630 of these neurons from individual brains into the AllenCCFv3 allows investigators to
631 study different neuron types within the same space and characterize their morphology
632 with respect to their transcriptomics. Mappings found between the fMOST image
633 and the AllenCCFv3 using our pipeline can be applied in this way to fMOST neuron
634 reconstruction point set data using `ants.apply_transforms_to_points(..)`.

635 **4.3 Mapping MERFISH data to AllenCCFv3**

636 **4.3.1 Preprocessing**

- 637 • *Initial volume reconstruction.* Alignment of MERFISH data into a 3-D atlas space
638 requires an estimation of anatomical structure within the data. For each section,
639 this anatomic reference image was created by aggregating the number of detected
640 genetic markers (across all probes) within each pixel of a $10 \times 10 \mu\text{m}^2$ grid to match
641 the resolution of the $10 \mu\text{m}$ AllenCCFv3 atlas. These reference image sections are then
642 coarsely reoriented and aligned across sections using manual annotations of the most
643 dorsal and ventral points of the midline. The procedure produces an anatomic image
644 stack that serves as an initialization for further global mappings into the AllenCCFv3.
- 645 • *Anatomical correspondence labeling.* Mapping the MERFISH data into the AllenCCFv3
646 requires us to establish correspondence between the anatomy depicted in the MERFISH

and AllenCCFv3 data. Intensity-based features in MERFISH data are not sufficiently apparent to establish this correspondence, so we need to generate instead corresponding anatomical labelings of both images with which to drive registration. These labels are already available as part of the AllenCCFv3; thus, the main challenge is deriving analogous labels from the spatial transcriptomic maps of the MERFISH data. Toward this end, we assigned each cell from the scRNA-seq dataset to one of the following major regions: cerebellum, CTXsp, hindbrain, HPF, hypothalamus, isocortex, LSX, midbrain, OLF, PAL, sAMY, STRd, STRv, thalamus and hindbrain. A label map of each section was generated for each region by aggregating the cells assigned to that region within a $10 \times 10\mu m^2$ grid. The same approach was used to generate more fine grained region specific landmarks (i.e., cortical layers, habenula, IC). Unlike the broad labels which cover large swaths of the section these regions are highly specific to certain parts of the section. Once cells in the MERFISH data are labeled, morphological dilation is used to provide full regional labels for alignment into the AllenCCFv3.

- *Section matching.* Since the MERFISH data is acquired as sections, its 3-D orientation may not be fully accounted for during the volume reconstruction step, due to the particular cutting angle. This can lead to obliqueness artifacts in the section where certain structures can appear to be larger or smaller, or missing outright from the section. To address this, we first use a global alignment to match the orientations of the MERFISH sections to the atlas space. In our pipeline, this section matching is performed in the reverse direction by performing a global affine transformation of the AllenCCFv3 into the MERFISH data space, and then resampling digital sections from the AllenCCFv3 to match each MERFISH section. This approach limits the overall transformation and thus resampling that is applied to the MERFISH data, and, since the AllenCCFv3 is densely sampled, it also reduces in-plane artifacts that result from missing sections or undefined spacing in the MERFISH data.

673 **4.3.2 2.5D deformable, landmark-driven alignment to AllenCCFv3**

674 After global alignment of the AllenCCFv3 into the MERFISH dataset, 2D per-section de-
675 formable refinements are used to address local differences between the MERFISH sections
676 and the resampled AllenCCFv3 sections. Nine registrations were performed in sequence us-
677 ing a single label at each iteration in the following order: 1) brain mask, 2) isocortex (layer
678 2+3), 3) isocortex (layer 5), 4) isocortex (layer 6), 5) striatum, 6) medial habenula, 7) lateral
679 habenula, 8) thalamus, and 9) hippocampus. This ordering was determined empirically by
680 an expert anatomist who prioritized which structure to use in each iteration by evaluat-
681 ing the anatomical alignment from the previous iteration. Global and local mappings are
682 then all concatenated (with appropriate inversions) to create the final mapping between the
683 MERFISH data and AllenCCFv3. This mapping is then used to provide a point-to-point
684 correspondence between the original MERFISH coordinate space and the AllenCCFv3 space,
685 thus allowing mapping of individual genes and cell types located in the MERFISH data to
686 be directly mapped into the AllenCCFv3.

687 **4.4 DevCCF velocity flow transformation model**

688 Given multiple, linearly or non-linearly ordered point sets where individual points across the
689 sets are in one-to-one correspondence, we developed an approach for generating a velocity
690 flow transformation model to describe a time-varying diffeomorphic mapping as a variant of
691 the landmark matching solution. Integration of the resulting velocity field can then be used
692 to describe the displacement between any two time points within this time-parameterized
693 domain. Regularization of the sparse correspondence between point sets is performed using
694 a generalized B-spline scattered data approximation technique⁸⁴, also created by the ANTsX
695 developers and contributed to ITK.

696 **4.4.1 Velocity field optimization**

697 To apply this methodology to the developmental templates¹⁶, we coalesced the manual an-
698 notations of the developmental templates into 26 common anatomical regions (see Figure 3).

699 We then used these regions to generate invertible transformations between successive time
700 points. Specifically each label was used to create a pair of single region images resulting in 26
701 pairs of “source” and “target” images. The multiple image pairs were simultaneously used to
702 iteratively estimate a diffeomorphic pairwise transform. Given the seven atlases E11.5, E13.5,
703 E15.5, E18.5, P4, P14, and P56, this resulted in 6 sets of transforms between successive time
704 points. Approximately 10^6 points were randomly sampled labelwise in the P56 template
705 space and propagated to each successive atlas providing the point sets for constructing the
706 velocity flow model. Approximately 125 iterations resulted in a steady convergence based
707 on the average Euclidean norm between transformed point sets. Ten integration points were
708 used and point sets were distributed along the temporal dimension using a log transform for
709 a more evenly spaced sampling. For additional information a help menu is available for the
710 ANTsPy function `ants.fit_time_varying_transform_to_point_sets(...)`.

711 4.5 ANTsXNet mouse brain applications

712 4.5.1 General notes regarding deep learning training

713 All network-based approaches described below were implemented and organized in the
714 ANTsXNet libraries comprising Python (ANTsPyNet) and R (ANTsRNet) analogs using
715 the Keras/Tensorflow libraries available as open-source in ANTsX GitHub repositories.
716 For the various applications, both share the identically trained weights for mutual re-
717 producibility. For all GPU training, we used Python scripts for creating custom batch
718 generators which we maintain in a separate GitHub repository for public availability
719 (<https://github.com/ntustison/ANTsXNetTraining>). These scripts provide details such as
720 batch size, choice of loss function, and network parameters. In terms of GPU hardware, all
721 training was done on a DGX (GPUs: 4X Tesla V100, system memory: 256 GB LRDIMM
722 DDR4).

723 Data augmentation is crucial for generalizability and accuracy of the trained networks.
724 Intensity-based data augmentation consisted of randomly added noise (i.e., Gaussian, shot,
725 salt-and-pepper), simulated bias fields based on N4 bias field modeling, and histogram warp-

726 ing for mimicking well-known MRI intensity nonlinearities^{46,96}. These augmentation tech-
727 niques are available in ANTsXNet (only ANTsPyNet versions are listed with ANTsRNet
728 versions available) and include:

- 729 • image noise: `ants.add_noise_to_image(...)`,
- 730 • simulated bias field: `antspynet.simulate_bias_field(...)`, and
- 731 • nonlinear intensity warping: `antspynet.histogram_warp_image_intensities(...)`.

732 Shape-based data augmentation used both random linear and nonlinear deformations in
733 addition to anisotropic resampling in the three canonical orientations to mimic frequently
734 used acquisition protocols for mice brains:

- 735 • random spatial warping: `antspynet.randomly_transform_image_data(...)` and
- 736 • anisotropic resampling: `ants.resample_image(...)`.

737 4.5.2 Brain extraction

738 Similar to human neuroimage processing, brain extraction is a crucial preprocessing step
739 for accurate brain mapping. We developed similar functionality for T2-weighted mouse
740 brains. This network uses a conventional U-net architecture⁹⁷ and, in ANTsPyNet, this
741 functionality is available in the program `antspynet.mouse_brain_extraction(...)`.
742 For the two-shot T2-weighted brain extraction network, two brain templates were gen-
743 erated along with their masks. One of the templates was generated from orthogonal
744 multi-plane, high resolution data⁶⁹ which were combined to synthesize isotropic volu-
745 metric data using the B-spline fitting algorithm⁸⁴. This algorithm is encapsulated in
746 `ants.fit_bspline_object_to_scattered_data(...)` where the input is the set of voxel
747 intensity values and each associated physical location. Since each point can be assigned
748 a confidence weight, we use the normalized gradient value to more heavily weight edge
749 regions. Although both template/mask pairs are available in the GitHub repository
750 associated with this work, the synthesized volumetric B-spline T2-weighted pair is available
751 within ANTsXNet through the calls:

- 752 • template: `antspynet.get_antsxnet_data("bsplineT2MouseTemplate")` and
753 • mask: `antspynet.get_antsxnet_data("bsplineT2MouseTemplateBrainMask")`.

754 **4.5.3 Brain parcellation**

755 The T2-weighted brain parcellation network is also based on a 3-D U-net architecture and the
756 T2-w DevCCF P56 template component with extensive data augmentation, as described pre-
757 viously. Intensity differences between the template and any brain extracted input image are
758 minimized through the use of the rank intensity transform (`ants.rank_intensity(...)`).
759 Shape differences are reduced by the additional preprocessing step of warping the brain ex-
760 tracted input image to the template. Additional input channels include the prior probability
761 images created from the template parcellation. These images are also available through the
762 ANTsXNet `get_antsxnet_data(...)` interface.

763 **Data availability**

764 All data and software used in this work are publicly available. The DevCCF atlas is
765 available at <https://kimlab.io/brain-map/DevCCF/>. ANTsPy, ANTsR, ANTsPyNet, and
766 ANTsRNet are available through GitHub at the ANTsX Ecosystem ([https://github.com/](https://github.com/ANTsX)
767 [ANTsX](#)). Training scripts for all deep learning functionality in ANTsXNet can also be
768 found on GitHub (<https://github.com/ntustison/ANTsXNetTraining>). A GitHub reposi-
769 tory specifically pertaining to the AllenCCFv3 mapping is available at <https://github.com/>
770 [dontminchenit/CCFAAlignmentToolkit](#). For the other two contributions contained in this
771 work, the longitudinal DevCCF mapping and mouse cortical thickness pipeline, we refer the
772 interested reader to <https://github.com/ntustison/ANTsXMouseBrainMapping>.

⁷⁷³ **Acknowledgments**

⁷⁷⁴ Support for the research reported in this work includes funding from the National Institute
⁷⁷⁵ of Biomedical Imaging and Bioengineering (R01-EB031722) and National Institute of Mental
⁷⁷⁶ Health (RF1-MH124605 and U24-MH114827).

777 Author contributions

778 N.T., M.C., and J.G. wrote the main manuscript text and figures. M.C., M.K., R.D., S.S.,
779 Q.W., L.G., J.D., C.G., and J.G. developed the Allen registration pipelines. N.T. and F.K.
780 developed the time-varying velocity transformation model for the DevCCF. N.T. and M.T.
781 developed the brain parcellation and cortical thickness methodology. All authors reviewed
782 the manuscript.

783 **References**

- 784 1. Keller, P. J. & Ahrens, M. B. Visualizing whole-brain activity and development at
the single-cell level using light-sheet microscopy. *Neuron* **85**, 462–83 (2015).
- 785 2. La Manno, G. *et al.* Molecular architecture of the developing mouse brain. *Nature*
596, 92–96 (2021).
- 786 3. Wen, L. *et al.* Single-cell technologies: From research to application. *Innovation
(Camb)* **3**, 100342 (2022).
- 787 4. Oh, S. W. *et al.* A mesoscale connectome of the mouse brain. *Nature* **508**, 207–14
(2014).
- 788 5. Gong, H. *et al.* Continuously tracing brain-wide long-distance axonal projections in
mice at a one-micron voxel resolution. *Neuroimage* **74**, 87–98 (2013).
- 789 6. Li, A. *et al.* Micro-optical sectioning tomography to obtain a high-resolution atlas of
the mouse brain. *Science* **330**, 1404–8 (2010).
- 790 7. Ueda, H. R. *et al.* Tissue clearing and its applications in neuroscience. *Nat Rev
Neurosci* **21**, 61–79 (2020).
- 791 8. Ståhl, P. L. *et al.* Visualization and analysis of gene expression in tissue sections by
spatial transcriptomics. *Science* **353**, 78–82 (2016).
- 792 9. Burgess, D. J. Spatial transcriptomics coming of age. *Nat Rev Genet* **20**, 317 (2019).
- 793 10. Hardwick, S. A. *et al.* Single-nuclei isoform RNA sequencing unlocks barcoded exon
connectivity in frozen brain tissue. *Nature biotechnology* **40**, 1082–1092 (2022).
- 794 11. Hawrylycz, M. *et al.* A guide to the BRAIN initiative cell census network data
ecosystem. *PLoS biology* **21**, e3002133 (2023).
- 795 12. Wang, Q. *et al.* The allen mouse brain common coordinate framework: A 3D reference
atlas. *Cell* **181**, 936–953.e20 (2020).
- 796 13. Perens, J. *et al.* An optimized mouse brain atlas for automated mapping and quantification
of neuronal activity using iDISCO+ and light sheet fluorescence microscopy.
Neuroinformatics **19**, 433–446 (2021).
- 797 14. Ma, Y. *et al.* A three-dimensional digital atlas database of the adult C57BL/6J mouse
brain by magnetic resonance microscopy. *Neuroscience* **135**, 1203–1215 (2005).

- 798 15. Qu, L. *et al.* Cross-modal coherent registration of whole mouse brains. *Nature Methods* **19**, 111–118 (2022).
- 799 16. Kronman, F. A. *et al.* Developmental mouse brain common coordinate framework. *bioRxiv* (2023) doi:[10.1101/2023.09.14.557789](https://doi.org/10.1101/2023.09.14.557789).
- 800 17. Chuang, N. *et al.* An MRI-based atlas and database of the developing mouse brain. *Neuroimage* **54**, 80–89 (2011).
- 801 18. Dries, R. *et al.* Advances in spatial transcriptomic data analysis. *Genome research* **31**, 1706–1718 (2021).
- 802 19. Ricci, P. *et al.* Removing striping artifacts in light-sheet fluorescence microscopy: A review. *Progress in biophysics and molecular biology* **168**, 52–65 (2022).
- 803 20. Agarwal, N., Xu, X. & Gopi, M. Robust registration of mouse brain slices with severe histological artifacts. in *Proceedings of the tenth indian conference on computer vision, graphics and image processing* 1–8 (2016).
- 804 21. Agarwal, N., Xu, X. & Gopi, M. Automatic detection of histological artifacts in mouse brain slice images. in *Medical computer vision and bayesian and graphical models for biomedical imaging: MICCAI 2016 international workshops, MCV and BAMBI, athens, greece, october 21, 2016, revised selected papers* 8 105–115 (Springer, 2017).
- 805 22. Tward, D. *et al.* 3d mapping of serial histology sections with anomalies using a novel robust deformable registration algorithm. in *International workshop on multimodal brain image analysis* 162–173 (Springer, 2019).
- 806 23. Cahill, L. S. *et al.* Preparation of fixed mouse brains for MRI. *Neuroimage* **60**, 933–939 (2012).
- 807 24. Sunkin, S. M. *et al.* Allen brain atlas: An integrated spatio-temporal portal for exploring the central nervous system. *Nucleic acids research* **41**, D996–D1008 (2012).
- 808 25. Kim, Y. *et al.* Brain-wide maps reveal stereotyped cell-type-based cortical architecture and subcortical sexual dimorphism. *Cell* **171**, 456–469 (2017).
- 809 26. Fürth, D. *et al.* An interactive framework for whole-brain maps at cellular resolution. *Nat Neurosci* **21**, 139–149 (2018).

- 810 27. Li, Y. *et al.* mBrainAligner-web: A web server for cross-modal coherent registration
of whole mouse brains. *Bioinformatics* **38**, 4654–4655 (2022).
- 811 28. Puchades, M. A., Csucs, G., Ledergerber, D., Leergaard, T. B. & Bjaalie, J. G. Spatial
registration of serial microscopic brain images to three-dimensional reference atlases
with the QuickNII tool. *PloS one* **14**, e0216796 (2019).
- 812 29. Eastwood, B. S. *et al.* Whole mouse brain reconstruction and registration to a ref-
erence atlas with standard histochemical processing of coronal sections. *Journal of
Comparative Neurology* **527**, 2170–2178 (2019).
- 813 30. Ni, H. *et al.* A robust image registration interface for large volume brain atlas. *Sci
Rep* **10**, 2139 (2020).
- 814 31. Pallast, N. *et al.* Processing pipeline for atlas-based imaging data analysis of struc-
tural and functional mouse brain MRI (AIDAmri). *Front Neuroinform* **13**, 42 (2019).
- 815 32. Celestine, M., Nadkarni, N. A., Garin, C. M., Bougacha, S. & Dhenain, M. **Sammbar-
MRI: A library for processing SmAll-MaMmal BrAin MRI data in python.** *Front
Neuroinform* **14**, 24 (2020).
- 816 33. Ioanas, H.-I., Marks, M., Zerbi, V., Yanik, M. F. & Rudin, M. **An optimized regis-
tration workflow and standard geometric space for small animal brain imaging.** *Neu-
roimage* **241**, 118386 (2021).
- 817 34. Perens, J. *et al.* Multimodal 3D mouse brain atlas framework with the skull-derived
coordinate system. *Neuroinformatics* **21**, 269–286 (2023).
- 818 35. Aggarwal, M., Zhang, J., Miller, M. I., Sidman, R. L. & Mori, S. Magnetic resonance
imaging and micro-computed tomography combined atlas of developing and adult
mouse brains for stereotaxic surgery. *Neuroscience* **162**, 1339–1350 (2009).
- 819 36. Goubran, M. *et al.* **Multimodal image registration and connectivity analysis for inte-
gration of connectomic data from microscopy to MRI.** *Nat Commun* **10**, 5504 (2019).
- 820 37. Chandrashekhar, V. *et al.* CloudReg: Automatic terabyte-scale cross-modal brain
volume registration. *Nature methods* **18**, 845–846 (2021).
- 821 38. Jin, M. *et al.* **SMART: An open-source extension of WholeBrain for intact mouse
brain registration and segmentation.** *eNeuro* **9**, (2022).

- 822 39. Negwer, M. *et al.* FriendlyClearMap: An optimized toolkit for mouse brain mapping
and analysis. *Gigascience* **12**, (2022).
- 823 40. Lin, W. *et al.* Whole-brain mapping of histaminergic projections in mouse brain.
Proceedings of the National Academy of Sciences **120**, e2216231120 (2023).
- 824 41. Zhang, M. *et al.* Spatially resolved cell atlas of the mouse primary motor cortex by
MERFISH. *Nature* **598**, 137–143 (2021).
- 825 42. Shi, H. *et al.* Spatial atlas of the mouse central nervous system at molecular resolution.
Nature **622**, 552–561 (2023).
- 826 43. Zhang, Y. *et al.* Reference-based cell type matching of in situ image-based spatial
transcriptomics data on primary visual cortex of mouse brain. *Scientific Reports* **13**,
9567 (2023).
- 827 44. Klein, S., Staring, M., Murphy, K., Viergever, M. A. & Pluim, J. P. W. Elastix: A
toolbox for intensity-based medical image registration. *IEEE Trans Med Imaging* **29**,
196–205 (2010).
- 828 45. Fedorov, A. *et al.* 3D slicer as an image computing platform for the quantitative
imaging network. *Magnetic resonance imaging* **30**, 1323–1341 (2012).
- 829 46. Tustison, N. J. *et al.* The ANTsX ecosystem for quantitative biological and medical
imaging. *Sci Rep* **11**, 9068 (2021).
- 830 47. Pagani, M., Damiano, M., Galbusera, A., Tsafaris, S. A. & Gozzi, A. Semi-automated
registration-based anatomical labelling, voxel based morphometry and cortical thick-
ness mapping of the mouse brain. *Journal of neuroscience methods* **267**, 62–73 (2016).
- 831 48. Anderson, R. J. *et al.* Small animal multivariate brain analysis (SAMBA) - a high
throughput pipeline with a validation framework. *Neuroinformatics* **17**, 451–472
(2019).
- 832 49. Allan Johnson, G. *et al.* Whole mouse brain connectomics. *Journal of Comparative
Neurology* **527**, 2146–2157 (2019).
- 833 50. Yao, Z. *et al.* A high-resolution transcriptomic and spatial atlas of cell types in the
whole mouse brain. *Nature* **624**, 317–332 (2023).

- 834 51. Bajcsy, R. & Broit, C. Matching of deformed images. in *Sixth International Conference on Pattern Recognition (ICPR'82)* 351–353 (1982).
- 835 52. Bajcsy, R. & Kovacic, S. [Multiresolution elastic matching](#). *Computer Vision, Graphics, and Image Processing* **46**, 1–21 (1989).
- 836 53. Gee, J. C., Reivich, M. & Bajcsy, R. [Elastically deforming 3D atlas to match anatomical brain images](#). *J Comput Assist Tomogr* **17**, 225–36 (1993).
- 837 54. Avants, B. B., Epstein, C. L., Grossman, M. & Gee, J. C. [Symmetric diffeomorphic image registration with cross-correlation: Evaluating automated labeling of elderly and neurodegenerative brain](#). *Med Image Anal* **12**, 26–41 (2008).
- 838 55. Klein, A. *et al.* [Evaluation of 14 nonlinear deformation algorithms applied to human brain MRI registration](#). *Neuroimage* **46**, 786–802 (2009).
- 839 56. Murphy, K. *et al.* [Evaluation of registration methods on thoracic CT: The EMPIRE10 challenge](#). *IEEE Trans Med Imaging* **30**, 1901–20 (2011).
- 840 57. Baheti, B. *et al.* [The brain tumor sequence registration challenge: Establishing correspondence between pre-operative and follow-up MRI scans of diffuse glioma patients](#). (2021).
- 841 58. Avants, B. B. *et al.* [The optimal template effect in hippocampus studies of diseased populations](#). *Neuroimage* **49**, 2457–66 (2010).
- 842 59. Avants, B. B., Tustison, N. J., Wu, J., Cook, P. A. & Gee, J. C. [An open source multivariate framework for n-tissue segmentation with evaluation on public data](#). *Neuroinformatics* **9**, 381–400 (2011).
- 843 60. Manjón, J. V., Coupé, P., Martí-Bonmatí, L., Collins, D. L. & Robles, M. [Adaptive non-local means denoising of MR images with spatially varying noise levels](#). *J Magn Reson Imaging* **31**, 192–203 (2010).
- 844 61. Tustison, N. J. *et al.* [N4ITK: Improved N3 bias correction](#). *IEEE Trans Med Imaging* **29**, 1310–20 (2010).
- 845 62. Wang, H. *et al.* [Multi-atlas segmentation with joint label fusion](#). *IEEE Trans Pattern Anal Mach Intell* **35**, 611–23 (2013).

- 846 63. Tustison, N. J. *et al.* Optimal symmetric multimodal templates and concatenated random forests for supervised brain tumor segmentation (simplified) with *ANTsR*. *Neuroinformatics* (2014) doi:[10.1007/s12021-014-9245-2](https://doi.org/10.1007/s12021-014-9245-2).
- 847 64. Tustison, N. J., Yang, Y. & Salerno, M. **Advanced normalization tools for cardiac motion correction**. in *Statistical atlases and computational models of the heart - imaging and modelling challenges* (eds. Camara, O. et al.) vol. 8896 3–12 (Springer International Publishing, 2015).
- 848 65. McCormick, M., Liu, X., Jomier, J., Marion, C. & Ibanez, L. **ITK: Enabling reproducible research and open science**. *Front Neuroinform* **8**, 13 (2014).
- 849 66. Beg, M. F., Miller, M. I., Trouvé, A. & Younes, L. **Computing large deformation metric mappings via geodesic flows of diffeomorphisms**. *International Journal of Computer Vision* **61**, 139–157 (2005).
- 850 67. Tustison, N. J. & Avants, B. B. **Explicit B-spline regularization in diffeomorphic image registration**. *Front Neuroinform* **7**, 39 (2013).
- 851 68. Hsu, L.-M. *et al.* CAMRI mouse brain MRI data.
- 852 69. Reshetnikov, V. *et al.* High-resolution MRI data of brain C57BL/6 and BTBR mice in three different anatomical views.
- 853 70. Rahman, N., Xu, K., Budde, M. D., Brown, A. & Baron, C. A. **A longitudinal microstructural MRI dataset in healthy C57Bl/6 mice at 9.4 tesla**. *Sci Data* **10**, 94 (2023).
- 854 71. Liu, J. *et al.* **Concordance of MERFISH spatial transcriptomics with bulk and single-cell RNA sequencing**. *Life Sci Alliance* **6**, (2023).
- 855 72. Stringer, C., Wang, T., Michaelos, M. & Pachitariu, M. **Cellpose: A generalist algorithm for cellular segmentation**. *Nat Methods* **18**, 100–106 (2021).
- 856 73. Jia, H., Yap, P.-T., Wu, G., Wang, Q. & Shen, D. Intermediate templates guided groupwise registration of diffusion tensor images. *NeuroImage* **54**, 928–939 (2011).
- 857 74. Tang, S., Fan, Y., Wu, G., Kim, M. & Shen, D. **RABBIT: Rapid alignment of brains by building intermediate templates**. *NeuroImage* **47**, 1277–1287 (2009).

- 858 75. Dewey, B. E., Carass, A., Blitz, A. M. & Prince, J. L. Efficient multi-atlas registration using an intermediate template image. in *Proceedings of SPIE—the international society for optical engineering* vol. 10137 (NIH Public Access, 2017).
- 859 76. Gong, H. *et al.* High-throughput dual-colour precision imaging for brain-wide connectome with cytoarchitectonic landmarks at the cellular level. *Nat Commun* **7**, 12142 (2016).
- 860 77. Wang, J. *et al.* Divergent projection patterns revealed by reconstruction of individual neurons in orbitofrontal cortex. *Neurosci Bull* **37**, 461–477 (2021).
- 861 78. Rotolo, T., Smallwood, P. M., Williams, J. & Nathans, J. Genetically-directed, cell type-specific sparse labeling for the analysis of neuronal morphology. *PLoS One* **3**, e4099 (2008).
- 862 79. Peng, H. *et al.* Morphological diversity of single neurons in molecularly defined cell types. *Nature* **598**, 174–181 (2021).
- 863 80. Chon, U., Vanselow, D. J., Cheng, K. C. & Kim, Y. Enhanced and unified anatomical labeling for a common mouse brain atlas. *Nat Commun* **10**, 5067 (2019).
- 864 81. Tasic, B. *et al.* Adult mouse cortical cell taxonomy revealed by single cell transcriptomics. *Nat Neurosci* **19**, 335–46 (2016).
- 865 82. Bergmann, E., Gofman, X., Kavushansky, A. & Kahn, I. Individual variability in functional connectivity architecture of the mouse brain. *Commun Biol* **3**, 738 (2020).
- 866 83. Billot, B. *et al.* SynthSeg: Segmentation of brain MRI scans of any contrast and resolution without retraining. *Med Image Anal* **86**, 102789 (2023).
- 867 84. Tustison, N. J. & Amini, A. A. Biventricular myocardial strains via nonrigid registration of anatomical NURBS model [corrected]. *IEEE Trans Med Imaging* **25**, 94–112 (2006).
- 868 85. Tustison, N. J. *et al.* Large-scale evaluation of ANTs and FreeSurfer cortical thickness measurements. *Neuroimage* **99**, 166–79 (2014).
- 869 86. Das, S. R., Avants, B. B., Grossman, M. & Gee, J. C. Registration based cortical thickness measurement. *Neuroimage* **45**, 867–79 (2009).

- 870 87. Tustison, N. J. *et al.* Longitudinal mapping of cortical thickness measurements: An Alzheimer's Disease Neuroimaging Initiative-based evaluation study. *J Alzheimers Dis* (2019) doi:[10.3233/JAD-190283](https://doi.org/10.3233/JAD-190283).
- 871 88. Grewal, J. S. *et al.* Brain gyration in wild and domestic canids: Has domestication changed the gyration index in domestic dogs? *J Comp Neurol* **528**, 3209–3228 (2020).
- 872 89. Avelino-de-Souza, K. *et al.* Anatomical and volumetric description of the guiana dolphin (*sotalia guianensis*) brain from an ultra-high-field magnetic resonance imaging. *Brain Struct Funct* (2024) doi:[10.1007/s00429-024-02789-1](https://doi.org/10.1007/s00429-024-02789-1).
- 873 90. Demirci, N., Hoffman, M. E. & Holland, M. A. Systematic cortical thickness and curvature patterns in primates. *Neuroimage* **278**, 120283 (2023).
- 874 91. Lerch, J. P. *et al.* Cortical thickness measured from MRI in the YAC128 mouse model of huntington's disease. *Neuroimage* **41**, 243–51 (2008).
- 875 92. Lee, J. *et al.* Automatic cortical thickness analysis on rodent brain. *Proc SPIE Int Soc Opt Eng* **7962**, 7962481–79624811 (2011).
- 876 93. Zöller, T., Attaai, A., Potru, P. S., Ruß, T. & Spittau, B. Aged mouse cortical microglia display an activation profile suggesting immunotolerogenic functions. *Int J Mol Sci* **19**, 706 (2018).
- 877 94. Avants, B. B. *et al.* The Insight ToolKit image registration framework. *Front Neuroinform* **8**, 44 (2014).
- 878 95. Avants, B. B. *et al.* A reproducible evaluation of ANTs similarity metric performance in brain image registration. *Neuroimage* **54**, 2033–44 (2011).
- 879 96. Nyúl, L. G., Udupa, J. K. & Zhang, X. New variants of a method of MRI scale standardization. *IEEE Trans Med Imaging* **19**, 143–50 (2000).
- 880 97. Falk, T. *et al.* U-net: Deep learning for cell counting, detection, and morphometry. *Nat Methods* **16**, 67–70 (2019).